A state-of-the-art review of micron scale spatially resolved residual stress analysis by ring-core milling and other techniques

A. J. G. Lunt[1], N. Baimpas[1], E. Salvati[1], I. P. Dolbnya[2], T. Sui[1], S. Ying[1], H.J. Zhang[1], A. Kleppe[2], J. Dluhoš[3], and A.M. Korsunsky[1 a)]

[1]*Department of Engineering Science, University of Oxford, Parks Rd, Oxford OX1 3PJ, UK*

[2] *Diamond Light Source, Harwell Science and Innovation Campus, Didcot, Oxfordshire OX11 0DE, UK*

[3] *TESCAN Brno, s.r.o., Libušina třída 1, 623 00 Brno, Czech Republic*

ABSTRACT

Quantification of residual stress gradients can provide great improvements in understanding the complex interactions between microstructure, mechanical state, mode(s) of failure and structural integrity. Highly focused local probe non-destructive techniques such as X-ray Diffraction (XRD), electron diffraction or Raman spectroscopy have an established track record in determining spatial variations of the *relative* changes in residual stress with respect to a reference state for many structural materials. However, the interpretation of these measurements in terms of *absolute* stress values requires a strain-free sample often difficult to obtain due to the influence of chemistry, microstructure or processing route. With the increasing availability of Focused Ion Beam (FIB) instruments, a new approach has been developed known as the micro-scale ring-core Focused Ion Beam - Digital Image Correlation (FIB-DIC). This technique is becoming the principal tool for quantifying the *absolute* in-plane residual stresses. It can be applied to a broad range of materials: crystalline and amorphous metallic alloys and ceramics, polymers, composites and biomaterials. The precise nanoscale positioning and well-defined

gauge volume of this experimental technique make it eminently suitable for *spatially resolved* analysis, i.e. residual stress profiling and mapping. In this review we first present a summary of this technique's background in the context of other micro-stress evaluation approaches. We then assess two recent applications of the spatially resolved FIB-DIC micro ring-core technique. The *sequential* ring-core milling FIB-DIC method allows micro- to macro-scale mapping at the step in the range 10-1000 μm, whilst the *parallel* FIB-DIC approach exploits simultaneous milling operation to quantify stress profiles at the micron scale (1-10 μm). Cross-validation against XRD results confirms that these approaches represent accurate, reliable and effective residual stress mapping methods.

[a)] Corresponding author. Electronic mail: *alexander.korsunsky@eng.ox.ac.uk*

Phone: 01865 273043

Keywords

- Residual stress
- Micro-scale
- Focused Ion Beam (FIB)
- Digital Image Correlation (DIC)
- Ring-core

INTRODUCTION

The need for accurate and reliable residual stress evaluation is well-established as a critical pre-requisite step in the understanding and prediction of engineering component behaviour and failure. The quantification of the magnitude and orientation, as well as the fine scale variation of the locked-in internal forces is of great utility for a wide range of applications, from studying the impact of ion radiation on thin films[1] to the interaction between residual and applied stresses contributing to the failure modes of high pressure components[2].

Residual stress analysis techniques can be classified into three main approaches:

1. *Non-destructive techniques.* Physical analysis methods allow residual stress evaluation via the quantification of small variations in structural or physical parameters e.g. the evaluation of the interplanar atomic lattice spacing by diffraction, or changes in molecular bond stiffness by spectroscopy. These methods have proven to be effective in determining the residual stress distributions at ultra-high resolution (down to tens of nm)[3, 4]. The physical basis of the approach is the interaction of particles or radiation (X-ray photons, neutrons, electrons) with the sample and a wide range of experimental methods have been developed. For example high resolution optical techniques [5-7] , Raman spectroscopy [8-11], electron back scatter diffraction [12-15], and a multitude of X-ray diffraction and spectroscopy techniques [16-21] have all been used to quantify the ***relative*** residual strain or stress distributions (i.e. with respect to a reference). The accuracy of all these measurement techniques is highly dependent upon the precision to which reliable reference values can be determined, a limiting factor which has been widely recognised in many of these studies.
2. *Stress analysis by material removal (destructive).* The introduction of traction-free surfaces by sample sectioning induces stress redistribution and strain relief in the surrounding

material. Quantification of this strain change can be used in combination with numerical modelling to back-calculate the stresses originally present in the material. Experimental techniques that rely upon this approach include the slitting and contour method[22-24], with a typical resolution in the range of fractions of a mm achievable.

3. *Semi-destructive stress analysis.* The introduction of localised stress relief through hole-drilling or core milling[25-27] can be used to quantify the magnitude of stress at a particular location ("point") within a sample. The quantification of the strain change induced at the surface is typically performed either using strain gauges, or by Digital Image Correlation (DIC) analysis. These measurements can then be used as inputs to enable back calculation of the stresses originally present. Traditional semi-destructive techniques are capable of resolving stress at the resolution of ~1 mm laterally, and at a depth resolution of ~0.03 mm.

The progressive refinement of these techniques has, in the last few years, provided methods for quantitative measurement of residual stress at resolutions down to a few microns. Whenever stress evaluation is discussed, it is worth recalling the definition of this complex tensor quantity. In the theory of solid continua, stress is defined using the components of internal material force acting across an imaginary sectional area, characterised by a certain orientation of its normal and size. This definition emphasises that stress is a *scale-dependent* quantity. Furthermore, dividing the internal force by the sectional area is equivalent to *averaging*, meaning that finer scale internal variation *must* be ignored in the analysis at the particular chosen scale. Experimental stress evaluation techniques are inextricably linked to a certain length scale, the so-called *gauge volume,* within which the interaction between the probe and the solid material in question is played out. Whenever reference is made to (residual) stress evaluation, the term *micron-scale* refers to a gauge volume with dimensions less than 10 μm in at least two of the three spatial

coordinates. In this context, depth profiling by chemical material removal (with steps down to a few microns) doesn't qualify as micron-scale measurement.

Recent studies have demonstrated that localised stresses (at the micron scale or even smaller) are often critical in the understanding of the origins and mechanisms of component failure. Unlike extrinsic properties such as stiffness, intrinsic properties of strength and fatigue resistance are dependent on the local "weakest link". This may be as small as a specific micron-sized region within a grain of material, at a grain boundary or junction. During service, it is the interaction between the residual stress and the applied load that determines the mechanical response and the likelihood of crack initiation. The interaction is played out over a wide range of different length scales, with the exact dominant dimension depending on the application. For example, it is customary to place principal emphasis on macro scale behaviour consideration in welding [28], micron scale in aero engine assemblies[29] and sub-micron scale in the case of nano-composites[30].

I. AN OVERVIEW OF X-RAY DIFFRACTION METHODS FOR MICROSCALE RESIDUAL STRESS ANALYSIS

Collimation of a parallel X-ray beam to define the illuminated region of the sample can be effective down to the spot size of approximately $10 \times 10\ \mu m^2$. Beam profiles smaller than this limit typically have insufficient flux to obtain diffraction profiles of the quality required for strain evaluation within a reasonable time period. Therefore, in order to reduce exposure times, tighter beam definition requires the use of focusing to improve the X-ray flux into the gauge volume. This tight focusing can be accomplished using either transmission optical elements, such as compound refractive lenses (CRLs) or Fresnel zone plates (FZPs), or reflective mirrors[31]. In recent years there has been growing interest in the development and use of optical elements such

as CRL-based transfocators[32] for high energy X-rays, and the use of diamond for making kinoform lenses[33].

Monochromatic diffraction micro-beam X-ray diffraction relies on obtaining a powder pattern from the gauge volume; therefore, the sample must have a fine-grained structure, with a sub-micron mean grain size. Debye-Scherrer patterns of coaxial scattering cones are typically collected on a 2D detector mounted either in the direct beam (transmission, Fig. 1), or on a side (reflection). Procedures and software can be used to reduce these 2D diffraction patterns to the more conventional one-dimensional profiles[34] which in turn can be analysed full profile refinement packages, such as FullProf[35], MAUD[36], or GSAS[37]. These patterns can be used to quantify the complete material strain state in the plane perpendicular to the incident beam[38], or as a measure of texture, i.e. orientation distribution function (ODF) analysis[39]. Nano-crystalline human dental tissues (dentine and enamel) is a prominent example of a natural material in which synchrotron diffraction characterisation has been applied to great effect [40-42].

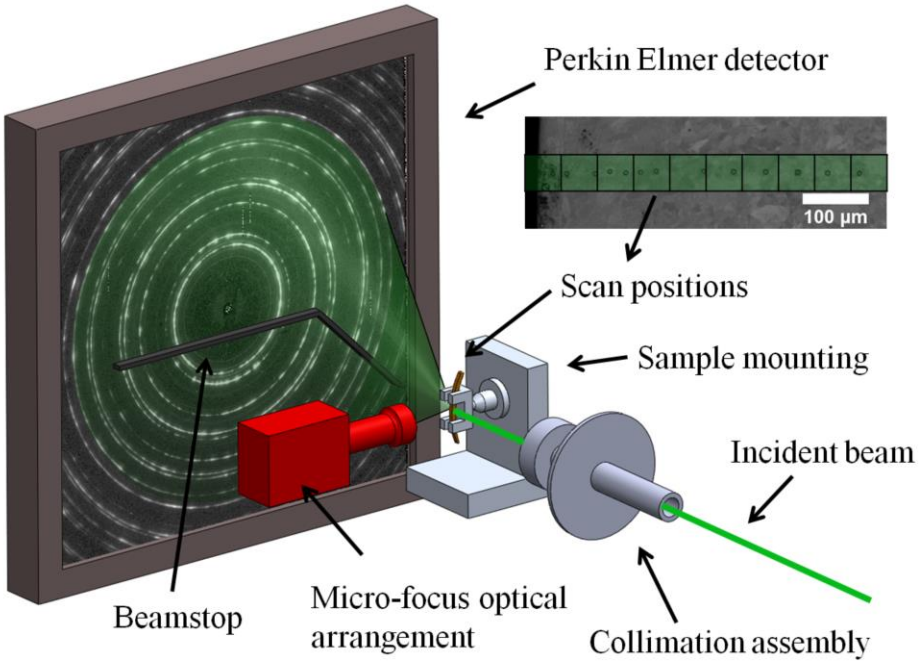

FIG. 1. Schematic representation of the synchrotron X-ray powder diffraction setup at beamline I15 (DLS, UK). X-ray diffraction patterns were collected by scanning the X-ray beam across the positions shown in the inset.

In larger grained ($< 20 - 30\ \mu m$) microstructures, micron-sized beams can be used to evaluate of intra-granular strains and stresses. Monochromatic analysis of this form presents a challenging need for precise rotational alignment between crystallographic orientation and incident beam, as well as micron scale sample positioning. An alternative is offered by the use of white beam (polychromatic radiation), also known as Laue mode diffraction, that can also be carried out in reflection[43] or transmission geometry[21]. The analysis of 2D Laue diffraction images can be accomplished using automated software tools to determine grain orientation and deviatoric lattice strain[44, 45]. Pure hydrostatic expansion or contraction of a unit cell does not change the angles between lattice planes, meaning that the Laue pattern does not alter, although the energies corresponding to individual reflections are modified. This effect can be registered using an energy resolving detector, or by filtering the incident beam energy[46]. Recent development of particular relevance to strain analysis concern careful evaluation of error sources[47], and the quantification of small distortion of Laue patterns due to lattice rotation and strain-induced distortion[48]. Recent Laue micro-diffraction studies include the evaluation of stresses promoting the growth of tin whiskers[49] and multi-technique mapping of deformation of nickel polycrystals[50] (Fig. 2).

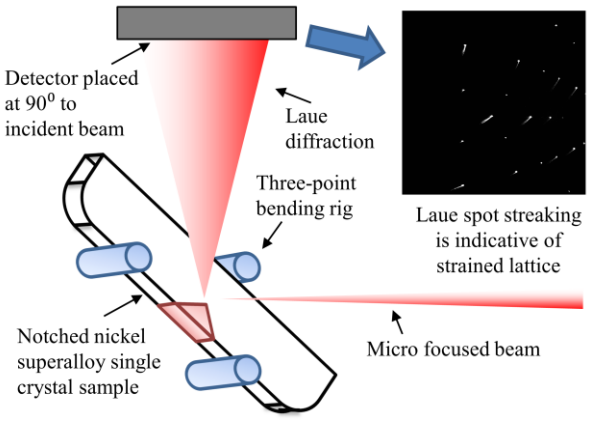

FIG. 2. Schematic of Laue diffraction during in-situ loading of a notched nickel superalloy single crystal

A final note should be made regarding studies attempting to use atomic Pair Distribution Function (PDF) analysis to determine strain in non-crystalline materials. The early paper by Poulsen et al.[51] opened the way to the development of this approach, while a more recent publication by Huang et al.[52] revealed the relationship between macroscopic strain and the shift in radial distribution peaks obtained from PDF analysis.

II. AN OVERVIEW OF ELECTRON DIFFRACTION TECHNIQUES FOR MICROSCALE RESIDUAL STRESS ANALYSIS

Electron diffraction provides another powerful route to determine lattice strains at resolutions ranging from the sub-micron scale in a back-scattered geometry, to a few nm in transmission.

Electron Back-Scatter Diffraction (EBSD), originally discovered by Nishikawa and Kikuchi in 1928, has grown in popularity since the advent of commercial Scanning Electron Microscope (SEM) in the 1960's. Automatic pattern indexing using the Hough transform[53] has since facilitated routine processing of large numbers of patterns. Grain orientation determination for microstructure mapping and micro-texture analysis are now popular applications of EBSD, along with the use of Kikuchi pattern quality assessment to visualise grain boundaries and plastically strained regions.

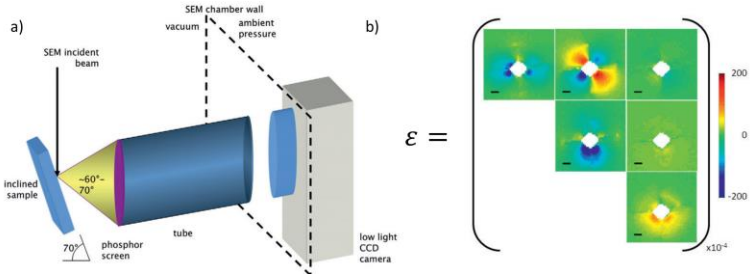

FIG. 3. a) Schematic diagram showing the experimental set-up for EBSD. b) EBSD elastic strain measurements around an indent in a silicon single crystal[12].

The classical angular resolution of EBSD lies in the range of $\sim 0.1^{\circ} - 0.5^{\circ}$, and therefore the determination of lattice strain (typically required at a resolution ~10^{-4}) appears to represent a

significant challenge using this technique. Nevertheless, in the last decade ever increasing levels of EBSD sensitivity have been achieved through the improvement of interpretation procedures. Accurate intragranular lattice mis-orientation and quantitative residual stress analysis is now possible by using DIC to quantify small changes in Kikuchi patterns (HR-EBSD) [12, 54] (Fig. 3).

High spatial resolution ($\sim$10 nm)[55] EBSD mapping has recently been published using a transmission geometry on thin samples such as TEM lamella[56]. This approach is similar to the high resolution strain mapping performed using TEM transmission diffraction e.g. using convergent beam diffraction[57]. In both of these cases, care must be taken to account for stress relaxation during lamella preparation[58].

III. SPECTROSCOPIC METHODS FOR MICRON SCALE RESIDUAL STRESS PROFILING

Spectroscopic techniques probe the atomic or molecular energetic characteristics of the sample in order to extract indirect information about residual stress state within the gauge volume. For example, peak shifts in Raman spectra can be related to the residual stress state within the volume illuminated by a monochromatic laser and confocal optics allow this beam to be focused to $\sim$0.2 μm. Furthermore, due to the penetration of light through the surface material layers, such setups facilitate residual stress depth profiling of micron-sized material volumes[59]. Raman spectroscopy residual stress mapping has recently been used to study zirconia-based thermal barrier coatings (TBC)[60] and the impact of etching on porous silicon[61] (Fig. 4). An important recent development in this field is correlative Raman and SEM imaging achieved by combining the two microscopy modes within one instrument[62].

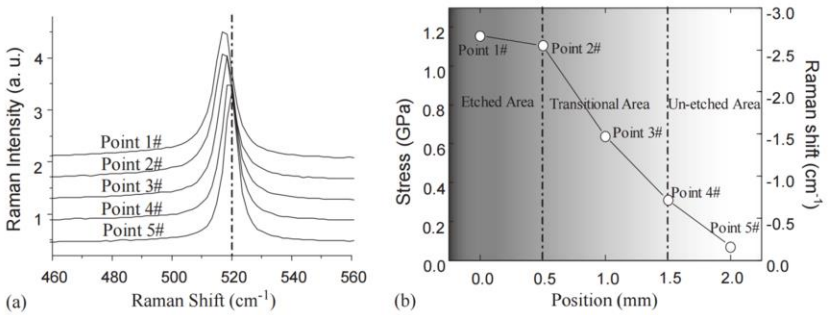

FIG. 4. Spatially resolved residual stress analysis in an etched surface of porous silicon[61]. The Raman peak shift detected at each location is shown in (a), and the corresponding residual stresses are shown in (b).

All the various modes of micron-scale stress evaluation described above, whilst benefiting from non-destructive nature, suffer from a number of limitations. Firstly, not all material types can be studied using these techniques: for example, diffraction only works with crystalline samples that contain grains of a size that can be approximated as either a powder or as a single crystal (relative to the beam size). Furthermore, diffraction of heavily deformed materials (e.g. metallic alloys) that contain significant lattice distortion, results in degraded diffraction patterns, making them impossible to interpret.

Spectroscopic methods such as Raman can only be applied to materials that contain molecular bonds. Consequently, polymers and oxides can be analysed in this way, whilst metallic alloys cannot.

Most importantly, all beam-based methods provide *relative* stress measurement, i.e. require a reference state for reliable interpretation. Providing reliable micron-sized reference volumes is known to formidably difficult in many samples of interest.

In contrast, techniques for stress evaluation based on material removal (e.g. slitting, sectioning, drilling) do not suffer from the above limitations: they can be applied to both amorphous and crystalline materials, including after heavy plastic deformation. Furthermore, experimental studies[3] and numerical simulation[63] have demonstrated the micro ring-core method

provides “on-board”, built-in reference. This approach not only provides a reference for quantitative interpretation of diffraction and spectroscopy data, but allows the determination of *absolute* residual stress state.

IV. MICRO RING-CORE DRILLING AND RELATED TECHNIQUES FOR RESIDUAL STRESS PROFILING

The idea of obtaining a minimally destructive probe of local residual stress using a ring-core geometry is not new: it goes back to the pioneering work of Keil in the early 1990’s[27]. The surge of recent interest is based on work by Korsunsky et al.[63], in which micro-scale Focused Ion Beam (FIB) ring-core milling was used to quantify residual stress in a precisely defined gauge volume. This broadly applicable basis has facilitated the development of a range of similar related techniques[64]. These methods rely on the introduction of new traction-free surfaces with quantification of the resulting surface strain relief. SEM images of the surface are typically post-processed using Digital Image Correlation (DIC) analysis software in order to quantify such changes. Comparison with Finite Element (FE) simulations is then used to relate this strain relief measurement to the pre-existing residual stress value.

One of the main limitations on the resolution of these semi-destructive techniques is the residual stress locally induced by ion implantation[65]. The magnitude and region of this influence is dependent upon the milling geometry, ion energy and material of interest[66]. Typically this zone is in the range of $10 - 100\ nm$ and therefore this acts as limit to FIB based stress quantification.

Micro-scale versions of the traditional macroscopic semi-destructive analysis techniques have been shown to be effective for quantifying fine scale residual stress, e.g. using slot milling[67] and hole drilling[25]. FIB based micro-slitting was first published by Kang et al.[68] in 2003 and has since become widely used to estimate residual stress in a direction perpendicular to the slit [69-71].

Recent improvements have provided estimates of residual stress variation with depth[64] and along the length of the slit[72]. Micro-scale FIB hole drilling, on the other hand, has provided estimates of the 2D stress state in a number of applications[73] including incremental depth resolved analysis[74] and spatially resolved investigations[75]. The main limitation of these approaches is that they rely on the strain relief induced in relatively large surface regions (typically ≥10's of microns). This means that the exact region of the stress evaluation is often difficult to pinpoint, and the spatial resolution is consequently reduced. In turn, this somewhat limits their applicability for high resolution spatially resolved analysis i.e. marker interaction is guaranteed at very small length scales ($< 10\ \mu m$).

Novel FIB approaches based on the uplift or in-plane relief of surface material have recently been proposed to quantify the plane stress state; these include the micro cantilever[76] and H bar[77] methods. The relatively long sample preparation times and limited measurement positions associated with these techniques means that they have limited relevance for stress mapping.

The ring-core FIB-DIC methodology allows quantification of the complete in-plane residual stress state at the micro-to-nano scale[63, 78-82]. This technique relies on inducing and measuring the strain relief within a well-defined gauge volume: a micro-pillar which is FIB milled in the material surface down to a depth-to-diameter aspect ratio ~1. The high speed, ease of application, precision and nanometre placement accuracy of this approach has meant that it has been applied to a wide range of materials and problems.

The use of a small island defines a precise gauge volume, but limits the area over which DIC can be performed. Despite this restriction, repeated imaging of the island surface provides a more thorough record of the strain change as a function of milling depth. The strain relief profile is then fitted with a "master curve" based on the results of previous FE simulations of the milling

process[83]. This approach means that FE analysis is not required, and quantitative results are obtained in minimal time.

Recent advances in this technique have demonstrated that depth-wise spatially resolved analysis can be implemented using the FIB-DIC approach [84]. Although the theoretical framework for this depth profiling is well-established and robust, experimental practicalities such as ion implantation, surface roughness and degradation and material inhomogeneity[85] impact the results of this approach. Therefore, attempts to declare residual stress depth profile measurements must be treated critically and by validation against the limited number of comparable techniques.

Alongside the review of the available micro-scale residual stress measurement techniques, the present paper assess the robustness and validity of the FIB-DIC methods to quantify in plane spatially resolved residual stress through the ring-core approach. Two possibilities arise for attaining this objective, namely, ***sequential milling*** or ***parallel milling*** of features on the sample surface. A schematic of these two approaches is shown in Fig. 5; *sequential* milling involves the incremental determination of residual stress in islands placed at regular intervals (left of Fig. 5), whereas *parallel* milling requires simultaneous milling of multiple features in a contiguous array (right of Fig. 5)

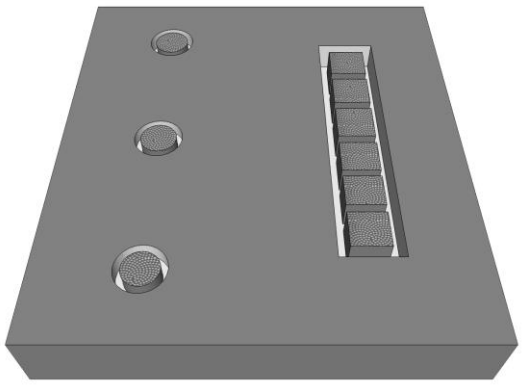

FIG. 5. A schematic of the *sequential* (left) and *parallel* (right) FIB-DIC milling approaches.

V. FUNDAMENTALS: THE SEQUENTIAL SPATIALLY RESOLVED RING-CORE FIB-DIC RESIDUAL STRESS ANALYSIS TECHNIQUE

Spatially resolved residual stress analysis offers obvious advantages over single point measurements, through their capacity to the reveal stress gradients. This lateral resolution is necessary to improve understanding of the interactions between microstructure, processing route and stress state in a range of materials and assemblies[86-88]. In order to ensure precise knowledge of the stress analysis location and to ensure a consistent gauge volume, a combination of microscopy and measurement is necessary in spatially resolved techniques. For these reasons the micro-scale ring-core FIB-DIC technique has excellent potential for use in spatially resolved analysis.

Direct comparison between the initial (undisturbed and residually stressed) and final (milled and strain relieved) states is needed for reliable semi-destructive stress analysis. In order to enhance the robustness of this interpretation, an incremental strain relief curve is often used[63, 77, 89]. The same approach can be implemented sequentially, provided successive measurements do not influence each other. This places a lower limit on the distance between successive milled features. The ring-core FIB-DIC technique introduces annular traction-free surfaces which induces stress (and therefore strain) relief in the surrounding region. Therefore, care must be taken to quantify the distance over which this variation becomes negligible.

To obtain an estimate of this lower limit, calculations on the basis of the classical Lamé thick-walled cylinder solution can be used. Consider the outer surface of the trench r_T as the inner surface of an infinitely thick cylinder in a state of equi-biaxial, uniform in-plane stress σ_R. The radial stress (σ_{rr}) and hoop stress ($\sigma_{\theta\theta}$) distributions can be written in a general form as[90] :

$$\sigma_{rr} = C - \frac{D}{r^2}, \tag{1}$$

$$\sigma_{\theta\theta} = C + \frac{D}{r^2}, \tag{2}$$

where the variable r represents the radial coordinate, and C and D are undetermined constants. The traction free surface at a radius r_T and constant residual stress σ_R state at an infinite distance are used as boundary conditions to determine C and D such that:

$$\sigma_{rr} = \sigma_R \left[1 - \left(\frac{r_T}{r}\right)^2\right], \tag{3}$$

$$\sigma_{\theta\theta} = \sigma_R \left[1 + \left(\frac{r_T}{r}\right)^2\right]. \tag{4}$$

This simplified stress analysis provides sufficient insight to conclude that the residual stress variation surrounding an annular feature is inversely proportional to the square of the ratio between the radial coordinate and the outer radius of the feature. By comparing the full through depth relief in a thick walled cylinder and the limited milling depth (~r_T) of the ring-core FIB-DIC approach, it can be seen that this approximation is an overestimate of the actual stress relief. This means that at a radius equal to five times island diameter, the induced stress change is guaranteed to fall below 1%.

VI. CASE STUDY: SEQUENTIAL SPATIALLY RESOLVED RESIDUAL STRESS ANALYSIS IN A SHOT PEENED AERO ENGINE COMPRESSOR BLADE

In order to provide a quantitative illustration of the capabilities of the *sequential* ring-core approach, an example study has been selected: a material surface response to shot peening. The residual stress profile induced by shot peening has been well characterised by a wide range of previous studies[91-94]. The form of a typical shot peened distribution is highlighted in Section VI.D with the exact residual stress profile depending on the shot peening parameters applied.

The sample selected for the present study was cut from an aero engine compressor blade made from nickel superalloy IN718. Careful control of the processing route resulted in a microstructure of sub-micron precipitates of γ' phase $Ni_3(Al,Ti)$ within an intermetallic face-centred-cubic austenitic phase γ matrix. Despite the highly anisotropic nature of grains within Ni-based superalloys, the microstructure was sufficiently refined to approximate the material as a polycrystalline under the scale of observation (~5 μm). The validity of this approximation was demonstrated by the similarity between the experimental strain relief profiles and the homogenous, isotropic, FE simulations (Fig. 6d)[63].

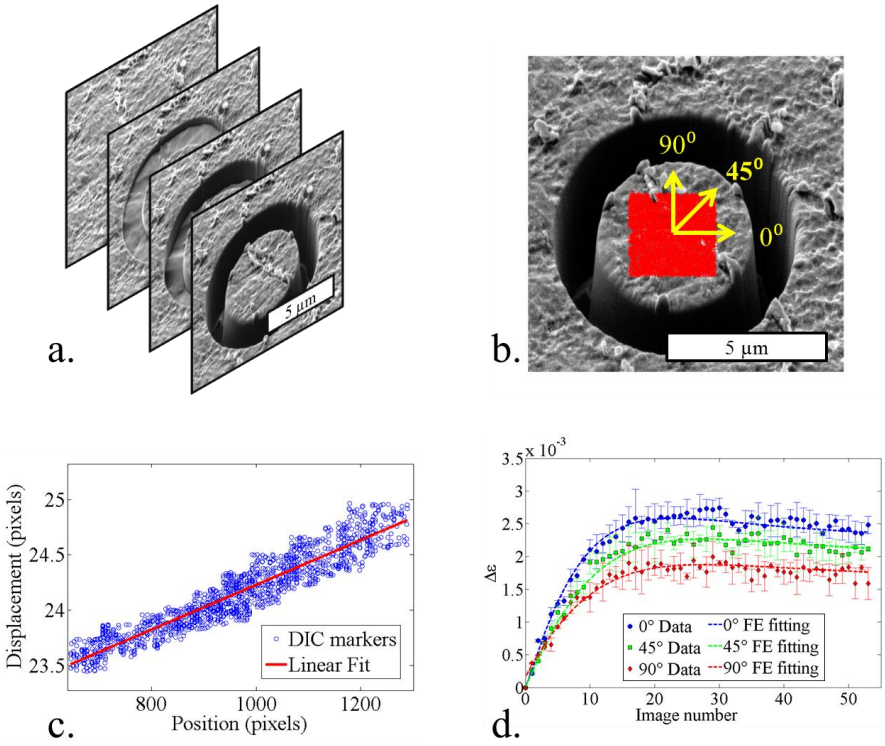

FIG. 6. Steps required to quantify full depth strain relief in the ring-core approach. a) Incremental collection of SEM images during milling. b) DIC marker tracking on the central core region (markers shown in red). c) Gradients of the displacement against position plots provide strain estimates at each milling depth. d) Strain relief analysis is performed in three directions (0°, 45° and 90°). The error bars represent 95% confidence intervals and the fitting function is given in Equation 5.

A. Sample Preparation

To ensure a consistent interaction, shot peening was applied to the entire surface of the compressor blade in a direction perpendicular to the blade. The affected depth was known to be significantly less than 1 mm; beyond the resolution of traditional macro-scale techniques. The ring-core FIB-DIC approach was sequentially implemented to form a line of milled annular features extending from the blade surface to approximately 520 μm into the bulk.

The sample was cut prior to analysis to expose a cross-section of the blade surface. In order to minimise any induced residual stress, a diamond saw (Buehler Isomet) was used to cut a 3 mm section of the blade and incremental grinding and polishing was used to further reduce the impact of any residual stresses induced by this process. As a final sample preparation stage, the polished cross-section was etched with Kalling's No. 1 reagent for 60 s. This revealed the γ and γ' distribution in the microstructure of underlying material and greatly increased the contrast of the SEM images of the surface, both in terms of surface roughness and Z-contrast. This property is important in the DIC procedures associated with this experimental approach.

B. The *Sequential* FIB-DIC Approach

The ring-core FIB-DIC approach was performed in the Tescan Lyra 3XM FIB-SEM instrument at the Multi-Beam Laboratory for Engineering Microscopy (MBLEM), Oxford, UK. Optimisation of the SEM parameters was used to generate a spot size of 6.9 nm and an automated contrast and brightness routine was used to maximise the dynamic range of the captured images. An image size of 2001×2001 pixels was selected as a compromise between high resolution imaging and experiment duration (and the associated potential for sample drift). Optimisation of FIB parameters was then performed to generate an effective spot size of 7.5 nm at a beam current of 100pA which was selected to reduce ion irradiation in the core.

An island diameter of 5 μm was chosen as a balance between milling time (longer for larger diameters) and the precision of stress evaluation (better for larger diameters). A trench width of 1.5 μm was selected to minimise the impact of re-deposited material onto the island surface and a nominal milling step of 100 nm was then used as an input into the automated incremental FIB milling script. Between each increment, SEM imaging of the core region was performed at an oblique angle of 55°. Tilt correction was used to decrease the vertical scanning increment in the SEM by a factor equal to $1/\cos 55°$, to ensure that the vertical and horizontal imaging resolution was equal. Milling was performed to a nominal depth of 5.3 μm in order to ensure that complete stress relief was obtained in the central island. The entire process took approximately 45 minutes and generated a total of 54 images.

Due to edge rounding, the first milling feature was placed approximately 20 μm from the edge. This process was then repeated 10 times along a line perpendicular to the surface in steps of approximately 50 μm. This spacing was chosen to ensure negligible marker interaction, while providing sufficient resolution to resolve the impact of shot peening. Difficulties in alignment and beam drift meant that some stress analysis points were unsuccessful. For this reason some features were placed closer together and others further apart (Fig. 7). The closest markers were placed 25 μm apart which corresponds to a maximum potential residual stress deviation of 2.5%.

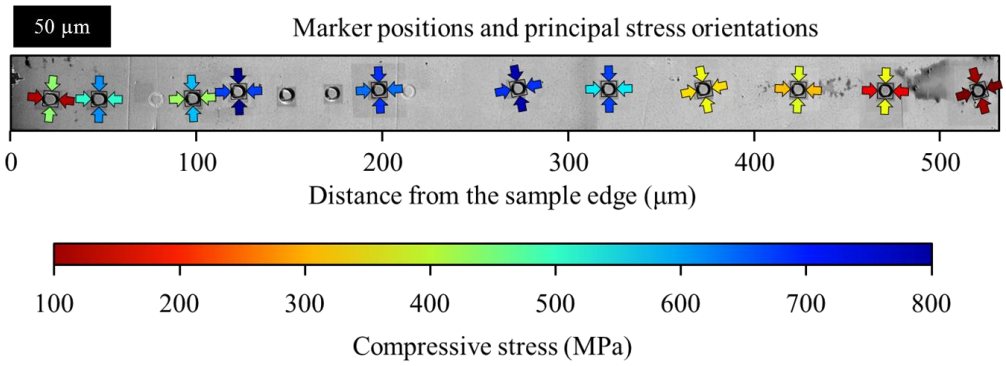

FIG. 7. Diagrammatic representation of the magnitude (arrow colour) and orientation (arrow rotation) of the principal stresses over an SEM image of the final milling positions.

After SEM image, DIC was performed on the core central region (where constant strain variation is expected[85]) using a modified version of a freely available DIC script[95] (Fig. 6b). Bulk drift was initially removed by performing lower resolution DIC and correcting for the shifts observed. Following manual and automated outlier removal, the well-tracked markers were used for the next stage of analysis.

Plots of displacement (Δx) against position (x) were then calculated for each image (Fig. 6c) and least squares fitting of a linear profile was used to quantify strain relief (as the gradient $\Delta\varepsilon = \Delta x/x$) in the 0°, 45° and 90° directions. Estimates of the $\Delta\varepsilon$ 95% confidence intervals were simultaneously obtained from the covariance matrix of this fitting process. A typical output data set from the feature placed at 115 μm from the surface is shown in Fig. 6d

The nominal "master curve" previously outlined by Korsunsky et al.[63] was then used to perform least squares fitting of the resulting profiles. This fitting process provides an estimate for the complete strain relief at an infinite milling depth ($\Delta\varepsilon_\infty$). However, to accommodate for minor variations in the milling rate and surface roughness, two further parameters were introduced. Parameter η below represents the apparent milling depth per image. Setting it to a constant implies that the milling depth h is directly proportional to the image number I. Parameter δ accounts for a minor offset in the milling depth, e.g. due to surface roughness. The final form was therefore,

$$f(\Delta\varepsilon_\infty, \eta, \delta) = 1.12\Delta\varepsilon_\infty \times \frac{z}{(1+z)}\left[1 + \frac{2}{(1+z^2)}\right], \qquad z = \frac{\eta I}{0.42d} + \delta, \tag{5}$$

where d is the diameter of the island (5 μm). The inverse of the standard deviation of the strain relief estimates were used as data point weightings in the least squares fitting approach. This enabled accurate estimates to be obtained for the 0°, 45° and 90° strain relief at infinite depths ($\Delta\varepsilon_\infty^{0^\circ}, \Delta\varepsilon_\infty^{45^\circ}$ and $\Delta\varepsilon_\infty^{90^\circ}$ respectively), as well as the standard deviation of these values.

Next, the principal strain relief orientations, magnitudes and standard deviations were determined ($\Delta\varepsilon_\infty^1$ and $\Delta\varepsilon_\infty^2$) from the 0°, 45° and 90° strain relief values. The microstructural directionality induced by the shot peening and surface milling ensured that the principal directions were closely aligned to the directions parallel and perpendicular to the sample edge, with an average offset of less than 4° (Fig. 7).

The principal strain relief values were then used to calculate the principal in-plane stress values (σ_1 and σ_2) and standard deviations at each marker location. This calculation was based on the non-equi-biaxial stress state expression previously outlined by Korsunsky et al.[63],

$$\sigma_1 = -\frac{E}{(1-\nu^2)}[\Delta\varepsilon_\infty^1 + \nu\Delta\varepsilon_\infty^2] \quad (6)$$

$$\sigma_2 = -\frac{E}{(1-\nu^2)}[\Delta\varepsilon_\infty^2 + \nu\Delta\varepsilon_\infty^1] \quad (7)$$

where E and ν are the bulk Young's modulus (205 GPa) and Poisson's ratio (0.294) values for IN718, respectively. This calculation is based on the assumption that the material is both isotropic and homogenous. Careful examination of the microstructure of the region of interest suggests that this is a valid approximation. However, any local variations in anisotropy would alter the stress results obtained. The extent of this alteration is the subject of ongoing analysis by means of numerical simulation[85].

C. X-ray Powder Diffraction Experimental Procedure

Following the sequential ring-core FIB-DIC residual stress analysis, X-ray Power Diffraction (XRPD) was performed at beamline I15 at Diamond light Source, UK using the experimental setup shown in Fig. 1. A $70 \times 70\ \mu m^2$ collimation assembly was used to define a pencil beam and a photon energy of 76 keV was selected to maximise the incident flux and diffraction signal from the sample.

The sample was placed into a specially manufactured mount and an optical alignment system was used to align the beam with the FIB-DIC marker locations with micron-scale precision. A raster scan was then used to collect diffraction patterns in increments of 50μm from the edge of the sample. A Perkin Elmer flat panel 1621-EN detector (2048×2048 pixels, pixel size 0.2×0.2 mm^2) was used to record the resulting diffraction patterns.

It was found that the relatively large crystallites present within the specimen induced graininess in the diffraction patterns (Fig. 1) and for this reason, 30° azimuthal integration was used to improve the grain sampling statistics of the resulting 1D spectra. A critical examination of the Debye-Scherrer rings revealed that sample graininess had least impact on the γ phase <200> peak. Lattice parameter quantification was therefore performed for the scattering vectors parallel and perpendicular to the interface for this peak.

D. Experimental Results

The variation in the principal stress magnitude and orientation determined by the *sequential* FIB-DIC approach is shown in Fig. 7. In general, compressive stresses in the range 100-500 MPa were observed near the sample edge. An increase in the magnitude of compressive stress is then observed towards a maximum of ~800 MPa at ~200 μm from the sample edge. The magnitude of the compressive stress then reduces to ~100 MPa at a 520 μm from the sample surface.

In order to aid in the visualisation of the stress distribution and provide comparison with the XRPD results, stresses in directions parallel and perpendicular to the interface were resolved (Fig. 8). The variation of these resolved components follows a very similar trend, with stresses in the perpendicular direction showing a marginally smaller magnitude. The interpretation of the results obtained using these two different techniques brings about with it the challenge of comparing conditions of plane strain (XRPD) and plane stress (surface FIB-DIC analysis).

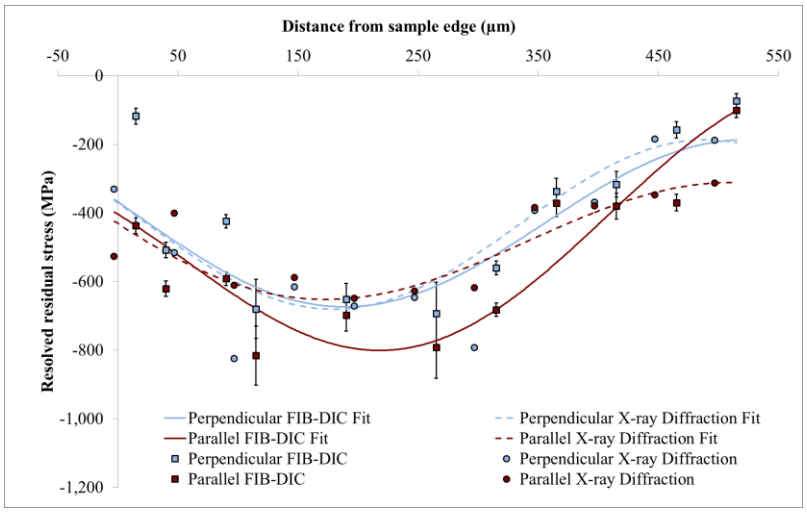

FIG. 8. FIB-DIC and X-ray diffraction residual stress estimates in directions parallel and perpendicular to the sample edge, against distance from the sample edge. The error bars indicate the 95% confidence intervals of each measurement. Least squares fitting of equation 12 has been used to highlight the average trends in the four profiles.

The plane problem of elasticity arises when deformation can be fully described in two-dimensional Cartesian coordinates. Let us consider a state of plane stress, in which x_3 is the direction of the surface normal. At the surface the out-of-plane stress components σ_{13}, σ_{23} and σ_{33} can be neglected. Strains due to the in-plane (residual) stresses can be written as [96]:

$$\varepsilon_{12} = \frac{2(1+\nu)}{E}\sigma_{12}, \qquad \varepsilon_{11} = \frac{1}{E}[\sigma_{11} - \nu\sigma_{22}], \qquad \varepsilon_{22} = \frac{1}{E}[\sigma_{22} - \nu\sigma_{11}]. \tag{8}$$

The only non-zero out-of-plane strain is found to be $\varepsilon_{33} = -\frac{\nu}{E}(\sigma_{11} + \sigma_{22})$.

Plane strain conditions arise if displacements everywhere in a solid body are perpendicular to the axis Ox_3, and do not depend on coordinate x_3. In this case the strain components ε_{13}, ε_{23}, ε_{33} vanish, $\sigma_{13} = \sigma_{23} = 0$, and $\sigma_{33} = \nu(\sigma_{11} + \sigma_{22})$. The strains are then given by:

$$\varepsilon_{12} = \frac{2(1+\nu)}{E}\sigma_{12}, \qquad \varepsilon_{11} = \frac{(1-\nu^2)}{E}\left[\sigma_{11} - \frac{\nu}{1-\nu}\sigma_{22}\right],$$
$$\varepsilon_{22} = \frac{(1-\nu^2)}{E}\left[\sigma_{22} - \frac{\nu}{1-\nu}\sigma_{11}\right]. \tag{9}$$

Note that equations (8) can be put into the form equivalent to (9), provided 'plane strain elastic constants' are introduced:

$$E' = \frac{E}{(1-\nu^2)}, \qquad \nu' = \frac{\nu}{1-\nu}. \tag{10}$$

Hence the term *plane problem of elasticity* can refer both to plane stress and plane strain.

For the purposes of our present analysis we adopt the approximation that cross section preparation results in the relief of the out-of-plane residual stress σ_{33}, but (to the first approximation) does not alter the residual elastic strains. This is consistent with the good agreement observed between the XRPD and FIB-DIC measurements.

For a given miller index hkl, the conversion between the XRPD lattice parameter variations (d_{hkl}) to estimates of lattice strain (ε_{hkl}), is given by:

$$\varepsilon_{hkl} = \frac{d_{hkl} - d^0_{hkl}}{d^0_{hkl}} \tag{11}$$

where d^0_{hkl} is the unstrained lattice parameter. In order to provide reliable measures of the *absolute* residual stress variation, accurate quantification of d^0_{hkl} is essential.

In this study a direct comparison between the *absolute* residual stress values obtained by FIB-DIC and *relative* values obtained by XRPD was used to find an optimal value for the unstrained lattice parameter of face centred cubic γ phase of IN718, $a^0_\gamma = 3.59756$ Å. This value corresponded well to existing literature values of a^0_γ [97, 98]. The least squares fitting approach implemented was also used to quantify the relative offset between the two profiles as $a^0 = 0.89939$ Å3.3 μm.

In order to facilitate effective comparison between the results, each profile was fitted with the shot peened residual stress profile originally proposed by Wantanbe et al. [99]:

$$\sigma_R = \alpha[\beta + \gamma z + \{1 + \cos(\theta z + \tau)\}] \tag{12}$$

where $\alpha, \beta, \gamma, \theta$ and τ are constants and z is the distance from the edge of the sample. This representation of the residual stress variation is valid up to the limiting depth of the plastic zone and the resulting profiles are shown in Fig. 8.

An indication of the 95% confidence intervals for the resolved FIB-DIC results has also been included in Fig. 8. These estimates require careful propagation of error values through multiple stages of least squares fitting and numerical calculations, and the average error was approximately +/-10% of the stress magnitude.

E. Discussion

The residual stress profiles obtained from the FIB-DIC and XRPD approaches reveal very similar distributions within the blade. Due to the relative offset between the techniques and the scatter of the data, the fitted profiles facilitate easier and more reliable comparison of the data. In the case of the perpendicular stress fitted curves, close proximities between the range of stress (493 MPa and 486 MPa), maximum compressive stress (680 MPa and 673 MPa), and location of this maximum stress (179 μm and 189 μm from the interface) were observed for the XRPD and FIB-DIC results, respectively. Greater differences were observed between the parallel stress distributions, however the general trends observed are still somewhat similar.

Local grain-to-grain variations in stress can be identified by the scatter around the fitted profiles. This behavior is known to be highly influential in crack propagation and sample failure[100] and previous ring-core FIB-DIC analysis has demonstrated that this technique is capable of capturing this intragranular variation[82].

In summary, the sequential spatially resolved ring-core FIB-DIC approach has been demonstrated to be an accurate, high resolution (micron-scale), in-plane residual stress analysis technique which has the potential to be applied to a wide range of problems. The main limitation of the *sequential* spatially resolved ring-core FIB-DIC residual stress analysis technique is the increment between subsequent strain measurements. An alternative approach, the *parallel* spatially resolved FIB-DIC approach, is introduced to overcome this limitation in Section VII.

VII. FUNDAMENTALS: THE PARALLEL SPATIALLY RESOLVED FIB-DIC RESIDUAL STRESS ANALYSIS TECHNIQUE

In order to increase the spatial resolution of the ring-core FIB-DIC approach, an alternative to the *sequential* approach, based on *parallel* milling of multiple cores, is proposed here. The *parallel* milling approach is based on simultaneously monitoring the strain relief in all cores with respect to the undisturbed state.

The central parameter of the ring-core FIB-DIC technique is the complete strain relief at the infinite milling depth ($\Delta\varepsilon_\infty$). This is the saturated value of the strain change induced in the surface of the milled island feature and is dependent only upon the residual stress state and the material parameters, and *not* on the milled feature geometry. Although the strain path between the undisturbed and fully relieved state depends on the milling process and the interactions between neighbouring features, the total strain change value $\Delta\varepsilon_\infty$ is invariant to these process changes. Continuous imaging of the relief, effective DIC and the attainment of a sufficient milling depth are all used to obtain the most reliable estimate of $\Delta\varepsilon_\infty$.

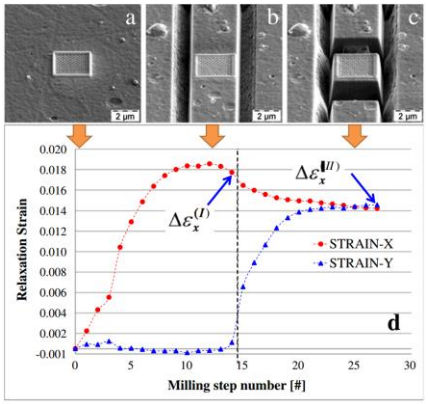

FIG. 9. Poisson's ratio determination at the micro-scale. a) DIC marker placement. b) Parallel vertical trench milling. c) Horizontal milling to leave a 3 µm fully relieved square island[89]

A recent paper by Sebastiani et al.[89], aimed at quantifying Poisson's ratio at the micro-scale, demonstrated the impact of alternative milling process routes on the surface relief in an equi-

biaxial-stressed thin film. Initially, two parallel vertical trenches were FIB milled in the surface (Fig. 9b). Following this, two further trenches were milled to leave a 3 μm square 'island' of relieved material (Fig. 9c). The strain relief variation in the vertical and horizontal directions was then used to estimate Poisson's ratio.

For the purposes of the present discussion we use the results of Sebastiani et al.[89] to consider the strain relief profiles as a function of depth, as shown in Fig. 9. Although the strain relief profiles in the two directions differ, the strain values converge at large milling depths. This proves that $\Delta\varepsilon_\infty$, is *robust*, i.e. will reach a magnitude that depends only on the undisturbed residual stress. It is known that the *parallel* milling approach will induce smaller variations in strain relief than those demonstrated by Sebastiani et al., and that a reliable estimate of $\Delta\varepsilon_\infty$, will therefore be obtained at large milling depths.

This complete stress relief results in an equivalence between the ring-core and square-core approach i.e. they will both enable reliable quantification of $\Delta\varepsilon_\infty$. Both techniques can therefore be used interchangeably depending on the specific user shape requirements.

In order to pursue parallel milling and imaging of multiple cores, a regular line of square features was implemented – the so-called "chocolate block" geometry (Fig. 10). This approach ensures that maximum lateral resolution of one marker width could be reached, with a regular step size between adjacent measurements, and is a much simpler milling regime than would be required to produce circular markers. Placing the markers close together also reduces the SEM field of view necessary to simultaneously capture all markers, thereby reducing the implementation time. The main limitation on the number of markers comes from the SEM imaging resolution achievable, i.e. the number of pixels that can be captured at the resolution necessary for accurate stress determination.

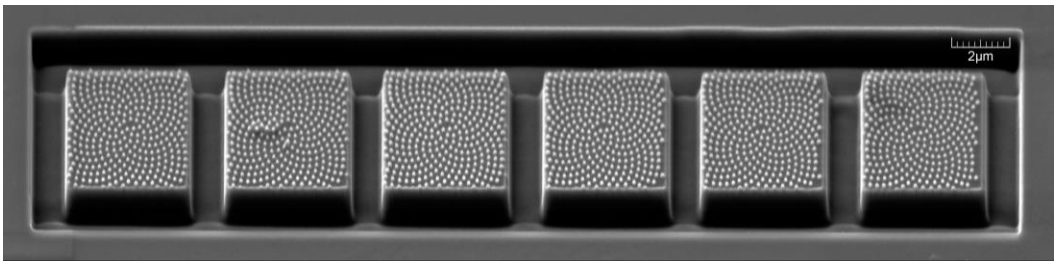

FIG. 10. SEM image of the *parallel* FIB-DIC milling arrangement – the "chocolate block" geometry. Electron deposition of markers has been used to increase the surface contrast of the cores. The average residual stress in the 4 μm cores was determined at an increment of 5 μm.

In order to guarantee reliable results the core centres must achieve a state of complete stress relief when milled in a regular arrangement, as proposed in this technique. Synchrotron XRPD mapping[3] has recently been used to demonstrate that this is valid for depth-diameter ratios greater than ~0.25 and therefore all milling has been performed to depth-diameter aspect ratios greater than 1.

In terms of the DIC analytical procedure, the *parallel* FIB-DIC approach is very similar to the *sequential* approach at each marker. The main difference is that the strain relief profile is no longer accurately described by the isolated ring-core feature due to the influence of neighbouring markers. Nevertheless, accurate estimates of $\Delta\varepsilon_{\infty}$ can be obtained, provided that the island is milled to a depth sufficient to induce full relief.

VIII. CASE STUDY: PARALLEL SPATIALLY RESOLVED RESIDUAL STRESS ANALYSIS IN A CARBON CORE SILICON CARBIDE FIBRE

Cross-validation between the results of a new experimental technique and a well-established method is a necessary step to assess result reliability. In this regard, a recent study of the residual strain distribution inside a carbon core silicon carbide (SiC) fibre was selected for comparison[101].

During this experiment XRPD was performed at beamline B16, at Diamond Light Source, Harwell, UK. High spatial resolution (400 nm) maps of lattice parameter variation were collected

across the carbon core and silicon carbide regions of the uniaxially reinforced titanium alloy (Ti-6Al-4V) composite. In order to convert this lattice variation into a measure of residual strain, accurate knowledge of the unstrained lattice parameter was required. Insurmountable difficulties arise in producing strain-free powder reference samples of these materials. Therefore, without the high spatial resolution (5 μm) analysis performed using the *parallel* FIB-DIC approach, only *relative* information on the strain variation could be obtained.

As previously highlighted, the strain relief obtained during the parallel FIB-DIC approach is a measure of *absolute* relief in the material surface. Therefore, after performing the necessary XRPD strain value averaging, the unstrained lattice parameters of the SiC and graphite core were obtained by direct comparison between the XRPD and the FIB-DIC strain profiles. Not only did this serve to cross-validate the two experimental techniques, but it also provided the necessary insight to ensure that the nano-scale strain variation determined by XRPD was a measure of *absolute* strain variation; the critical parameter in understanding the failure modes of these fibres.

At this point it is important to note that the back-calculation of the residual stress state must be performed with care due to the variations in amorphous content and associated anisotropy. Nevertheless, the *strain* profiles obtained by XRPD and the FIB-DIC approach can be compared, and show consistent results as outlined in Section VIII.D.

A. Sample Preparation

The SiC and titanium alloy composite in this study was comprised of 35% by volume SCS-6 SiC fibres aligned in a single direction. The fibre was composed of a 30 μm diameter graphite core which was surrounded by SiC with an outer diameter of 140 μm. Within this graphite core, a distinct untextured central 13.5 μm diameter region was observed. Two different lattice parameter values were therefore obtained for carbon, one for the inner and one for outer region.

In order to minimise the residual stresses induced during preparation sample sectioning was performed using a diamond saw (Buehler Isomet), this was followed by an incremental grinding and colloidal silica polishing process. A final thickness of ~500 μm was selected in order to maximise the diffracted beam intensity at the energies available at beamline B16.

As part of the experimental process outlined in our previous paper[3], tomographic reconstruction of the SiC was also performed. In order to facilitate full illumination of the sample by the X-ray beam, further sectioning was performed using a similar diamond saw and polishing process. The final sample was a $1\times0.5\times0.5$ mm^3 cuboid as shown in the insert in Fig. 11.

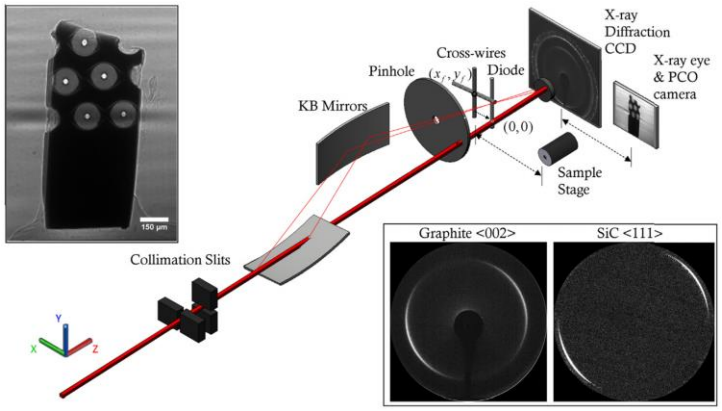

FIG. 11. Schematic of the XRPD setup showing the aligned sample and diffraction patterns from the SiC and graphite regions [101].

B. X-ray Powder Diffraction Experimental Procedure

In order to record the highly spatially resolved variations of elastic strain, the KB nano-scale focusing capabilities available at B16 were exploited to produce a 400×500 nm^2 beam. A 150 μm diameter pinhole was used to block the higher order reflections as shown in Fig. 11. The sample was placed on a translation and rotation stage and X-ray imaging was used to align the sample in a direction parallel to the incident beam. An incremental beam-alignment process was then implemented to determine the location of the beam on the sample surface to nano-scale accuracy, this is outlined in detail elsewhere[101].

Piezoelectric translation stages were used to raster the sample incrementally across the beam, and diffraction patterns were recorded at each location. Six line scans were implemented in order to map a representative region of the SiC and the carbon core.

Azimuthal integration of the resulting diffraction patterns was performed, and the lattice parameter variation was determined for scattering vectors pointing in the radial and hoop directions. The lattice parameter variation in each of the different regions was determined: a in the case of face centred cubic SiC and c, the larger unit cell dimension, for the hexagonal close packed graphite. As previously noted two different lattice constants were required in in the graphite; c_0 in the case of the outer textured region and c_i in the case of untextured the inner core region. The crystallographic texture associated with the SiC region limited the azimuthal angles over which a representative lattice constant could be quantified and therefore only the variation in the radial lattice constant was determined.

C. The *Parallel* FIB-DIC approach

Following XRPD, the sample was placed into the Tescan Lyra 3XM FIB-SEM instrument at MBLEM, Oxford. SEM parameter optimisation was performed to give a 5.7 nm spot size and an image size of 4096×4096 pixels was selected in order to maximise the resolution of the captured images. Careful focusing, line and image averaging, as well as automated contrast and brightness selection was used to maximise the dynamic range and reduce noise in the image.

One of the advantages of the ring-core technique is that during milling the core approaches a state of approximately uniform strain relief[85]. Assuming good image stability, this area averaging minimises the impact of image distortion on the strain estimate. This means that ring-core can be reliably implemented at lower magnification, e.g. compared to FIB-DIC techniques which rely upon the precise determination of displacement fields, such as hole drilling[102] or slitting[22].

The same FIB beam parameters were implemented as those outlined in Section VI.B. Both the SiC and carbon core were found to have similar FIB milling rates and therefore a single parallel milling process was implemented on both regions simultaneously. Six cores with dimensions of 4×4 μm^2 were selected as a compromise between maximising the number of stress evaluation points on one hand, and the precision of these estimates, on the other. A trench width of 1 μm was chosen in order to minimise the increment between successive points and a depth-diameter ratio of 1.27 was selected to ensure complete relaxation in the core. The stress analysis positions were located at radial distances between 2.5 μm and 27.5 μm from the fibre axial line, in increments of 5 μm, as shown in Fig 12.

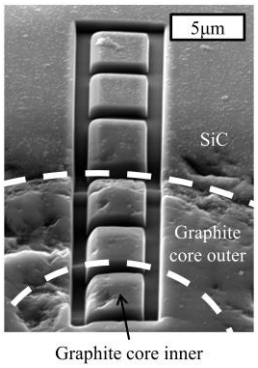

FIG. 12. SEM image of the *parallel* FIB-DIC technique in which the interfaces between the SiC region, the graphite core outer and the graphite core inner are highlighted. The core sizes are uniform in the direction of the global surface normal. However, slight variations in topology create the illusion of size variation. The Z-contrast induced by colloidal silica is also shown [101].

In order to overcome the limitations of SEM imaging, a very small FIB milling increment of 15 nm was selected. This minimises the strain change between successive measurements and increases the likelihood of effective DIC tracking. A small milling current of 100pA was selected to reduce the amount of material redeposition on the islands (and the associated image blurring in the DIC analysis) and to minimise the residual stress induced by gallium ion implantation.

The optimised arrangement captured 340 images over a period of approximately 5 hours. Although this time period may seem long, the full 2D in plane stress state is characterised at 6

different locations during this interval. Eighteen independent implementations of a 1D stress characterisation technique would be necessary to obtain comparable data, resulting in an equivalent time budget of 17 minutes per data point for the *parallel* FIB-DIC method.

DIC of the resulting images was performed using a modified version of the DIC script developed by Eberl[95]. It was found that the residual colloidal silica provided increased surface contrast thereby improving marker tracking effectiveness. Bulk drift was initially accounted for by performing lower resolution DIC and each core surface was tracked individually during six independent implementations of the script. Automated and manual outlier removal was used to retain only the well-tracked markers.

FIG. 13.

In this study, strain relief profiles were obtained in the radial and hoop directions for each of the 6 cores. Although theoretically possible, the full in-plane strain tensor was not quantified. This is due to the fact that unknown mechanical property variations prevent the conversion of the strain relief results into stress. Therefore, it was decided that full tensor analysis would offer limited value for the present study.

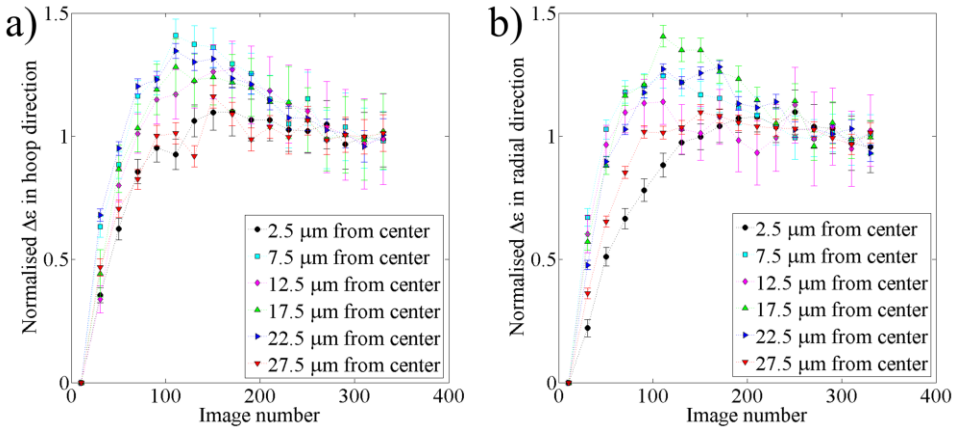

FIG. 14. Normalised strain relief twenty point weighted average against image number for the six stress analysis locations, in the hoop (a) and radial (b) directions.

Relatively high levels of noise (and the associated 95% confidence intervals) were observed in the profile of strain relief against the image number (i.e. milling depth). A weighted average of multiple (20) markers was therefore calculated based on the inverse of the standard deviation of each relief value. Following normalisation against the full depth strain relief values, the results of this averaging are shown in Fig. 13. The image number of each point was chosen as the central image number over which the strain relief values which had been averaged.

The first conclusion drawn from Fig. 13 is that milling has been performed to a depth sufficient to induce full relief in the cores. This is demonstrated by plateaus in all of the strain relief profiles.

The influence of neighbouring markers is also demonstrated in Fig. 13, through the slight differences observed in the strain relief profiles. Feature symmetry suggests that the profiles at 2.5 μm and 27.5 μm, 7.5 μm and 22.5 μm, and 12.5 μm and 17.5 μm should be similar. Careful examination of the profiles demonstrates a degree of similarity between these profiles.

Despite minor variations the strain relief profiles, the general variation is very similar to the functional form of the isotropic, single ring-core FE model in Equation 5. Based on this insight, careful least-squares fitting of this function was performed on the data. It is believed that minor variations in the near-surface relief profile should have a limited impact on the estimate of $\Delta\varepsilon_\infty$ obtained from this process. This is increasingly true for profiles for which a large milling depth has been reached. To provide additional support for this assumption, FE modelling of the *parallel* FIB-DIC feature geometry could be used. However, the authors are confident of the reliability of the approach, both from the theoretical point of view, and experience. This conclusion is supported by the agreement observed between the XRPD parallel FIB-DIC results.

D. Experimental Results

In order to interpret the SiC and graphite XRPD lattice parameter variation in terms of strain, accurate quantification of the unstrained lattice parameters was required. A least squares optimisation approach was therefore implemented starting from literature values of the unstrained lattice parameters (a^0= 4.3596 Å[103] for the face centred cubic SiC region and c^0=6.720 Å[104] for the larger unit cell dimension of the graphite region). For this analysis, averaging of the XRPD strain values over the relevant gauge volume was necessary to provide comparative values. For example, the FIB-DIC estimate at the 2.5 μm position represents a strain average between the radii of 0.5 μm and 4.5 μm. The optimised values were found to be a^0 = 4.3982 Å, c_o^0 = 6.8353 Å and c_i^0 = 6.9980 Å where the subscript 0 refers to the unstrained lattice parameters of the SiC (a), graphite outer region (c_0) and the graphite inner region (c_i) defined in Section VIII.D.

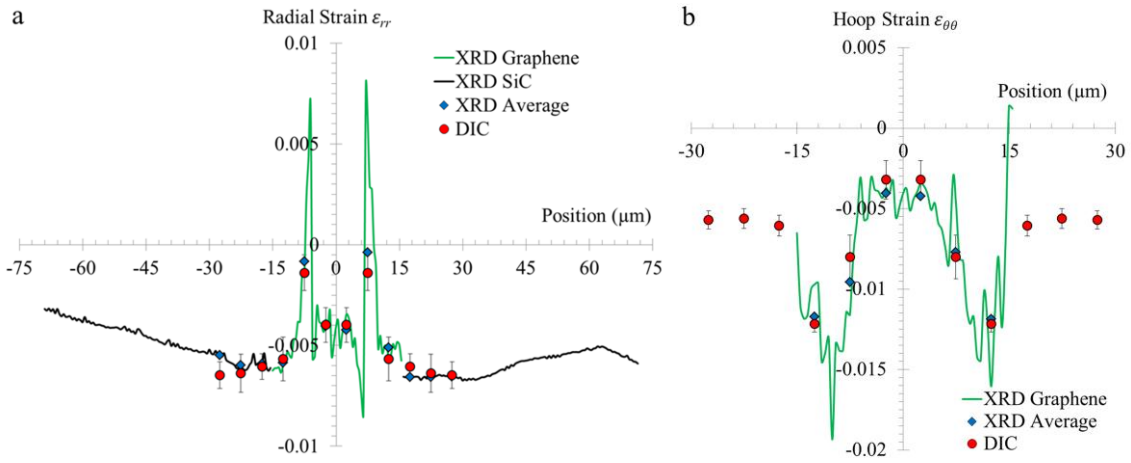

FIG. 15. Radial (a) and hoop (b) absolute strain distributions within the graphite and SiC regions of the core[101]. The results of both the XRPD and the *parallel* FIB-DIC are shown as well as the comparable average XRPD results. The 95% confidence intervals of the XRPD values are indicated by the error bars.

The variations in the *absolute* residual strain obtained from the XRPD and FIB-DIC approach are plotted together in Fig. 14. The SiC region can be seen to be in a state of compressive strain which decreases in magnitude at distances further from the core. The central carbon core region is in a state of approximate hydrostatic compressive strain of ~0.4%. The

outer carbon core, on the other hand, is in a state of dilatational strain; the radial component is tensile and the hoop strain is compressive.

E. Discussion

To calculate the confidence intervals of the FIB-DIC strain relief values, careful error propagation was performed through the multiple stages of least squares fitting. The expected differences between the strain relief profiles (Fig. 13) and the functional fitting distribution implemented (Equation 5), ensured that relatively large 95% confidence intervals were obtained, with an average confidence interval of +/- 20%.

Examination of the average XRPD data reveals that only three out of the eighteen data points fall outside the FIB-DIC 95% confidence bounds, and that the average percentile error is 13%. Taking into account the assumptions necessary to compare these two different techniques (Section VI.D), these two data sets show strong similarities in the distributions obtained. This suggests that the *parallel* spatially resolved FIB-DIC approach is a reliable method for in-plane absolute residual distributions of strain, and of stress in well-characterised materials.

The benefits of the *parallel* FIB-DIC approach can be demonstrated by critical comparison of with recent high spatial resolution analysis of residual stress using slotting based methods[72]. This approach employs a single slot to determine residual stress variation along the slot in a direction perpendicular to the slot. Although this is a marginally simpler experimental form, the requirement to repeatedly perform FE simulations and full displacement field characterisation ensures that processing time and complexity is higher than the *parallel* FIB-DIC approach. This full field characterisation also means that no strain averaging can be performed and therefore the impact of noise is larger. Further, the impact of edge effects at the end of the slot greatly reduces the precision of the slot based technique in these regions, especially when compared to the results shown in Fig. 14. Most importantly the ability to determine the full in plane stress tensor

using the *parallel* FIB-DIC approach, rather than the 1D stress state, enables much greater insight into the likely failure modes or stress interaction in the region of interest.

Despite the advantages of the *parallel* FIB-DIC technique its use is likely to be limited to specialised applications where micron-resolved residual stress analysis is crucial in improving current understanding. This restriction is primarily associated with the long milling times (~ 5 hours) although dramatically shorter milling times would be possible is less precise measurements of residual stress are required (increased milling rates typically reduce DIC accuracy). Other restrictions on the technique include the minimum resolution and maximum region over which stress can be assessed, very high resolution analysis ($< 1\ \mu m$) would likely begin to be influenced by the effects of ion implantation and reduced DIC areas, whereas limitations on maximum high resolution SEM image sizes and increased milling times place an upper boundary on the assessment region. Finally, as highlighted in the carbon fibre example study, difficulties in obtaining precise and reliable stiffness tensor matrices at these resolutions may provide challenges in the conversion of the strain relief values to residual stress estimates.

The elastic strain distributions evaluated during this study were used as the basis for further FE simulation of the SiC and carbon core region[101]. The insights obtained provided improved understanding of the impact of the processing route on the resulting microstructure and strain distributions. Of particular interest was the relatively high tensile strains observed at the interface between the carbon outer and carbon inner regions inside this complex hierarchical structure.

IX. CONCLUSIONS

Two differing methodologies have been presented to provide spatially resolved in-plane residual stress analysis based on the FIB-DIC principle. The well-defined gauge volume, the

possibility of component-specific stress analysis as well as the potential to access two different spatial length scales, mean that a highly versatile approach has been elaborated.

The *sequential* spatially resolved ring-core FIB-DIC approach has been shown to allow quantification of the residual stress state at a spatial resolution from the millimetre down to tens of micrometres, with micro-scale averages obtained at each point. A comparison between XRPD and this approach has demonstrated this technique produces reliable and consistent results. The main limitation of this approach is the interference observed when subsequent stress measurements are placed close together.

In order to overcome this limitation, the *parallel* FIB-DIC approach has been proposed. This technique involves simultaneous milling of multiple compact features (squares) in order to obtain residual stress estimates with a spatial resolution at the micro-scale, both in terms of the gauge volume and step. Cross-validation between the residual strain profiles obtained by high resolution XRPD and this approach suggests that, despite observing larger signal to noise ratios, this approach also offers a reliable and effective technique for spatially resolved residual stress.

In order to improve the reliability of these results further modelling of this technique could be performed, for example by performing FE simulations of the regions surrounding ring-core markers, or by quantifying the relief profiles expected at each of the feature positions in the *parallel* milling approach. Such insights may allow the markers to be placed closer together, or may improve the accuracy of strain profile fitting in the *parallel* approach.

Overall, the two newly proposed techniques are fast, robust and reliable. They offer the potential to perform spatially resolved residual stress analysis from the millimetre down to micrometre scale with nano-scale precision. It is hoped that their application to spatially resolved

residual stress problems will provide the insights required to understand material failure, the impact of processing or the influence of residual stress on mechanical properties.

ACKNOWLEDGEMENTS

The present work benefited from the support of G. Baxter, C. Heason, M. Jones and I. Mitchell from Rolls-Royce plc, who provided the shot-peened compressor blade sample as well as valuable assistance in the analysis of this case study.

REFERENCES

1. Misra A, Fayeulle S, Kung H, Mitchell TE and Nastasi M. Effects of ion irradiation on the residual stresses in Cr thin films. *Appl Phys Lett*. 1998; 73: 891-3.
2. Jeyakumar M and Christopher T. Influence of residual stresses on failure pressure of cylindrical pressure vessels. *Chinese Journal of Aeronautics*. 2013; 26: 1415-21.
3. Baimpas N, Le Bourhis E, Eve S, Thiaudière D, Hardie C and Korsunsky AM. Stress evaluation in thin films: Micro-focus synchrotron X-ray diffraction combined with focused ion beam patterning for do evaluation. *Thin Solid Films*. 2013; 549: 245-50.
4. Singh DRP, Deng X, Chawla N, et al. Residual stress characterization of Al/SiC nanoscale multilayers using X-ray synchrotron radiation. *Thin Solid Films*. 2010; 519: 759-65.
5. Ye C, Telang A, Gill AS, et al. Gradient nanostructure and residual stresses induced by Ultrasonic Nano-crystal Surface Modification in 304 austenitic stainless steel for high strength and high ductility. *Materials Science and Engineering: A*. 2014; 613: 274-88.
6. Javadi Y, Sadeghi S and Najafabadi MA. Taguchi optimization and ultrasonic measurement of residual stresses in the friction stir welding. *Materials & Design*. 2014; 55: 27-34.
7. Karabutov A, Devichensky A, Ivochkin A, et al. Laser ultrasonic diagnostics of residual stress. *Ultrasonics*. 2008; 48: 631-5.
8. Chen S-l, Shen B, Zhang J-g, Wang L and Sun F-h. Evaluation on residual stresses of silicon-doped CVD diamond films using X-ray diffraction and Raman spectroscopy. *T Nonferr Metal Soc*. 2012; 22: 3021-6.
9. Nibennanoune Z, George D, Antoni F, et al. Improving diamond coating on Ti6Al4V substrate using a diamond like carbon interlayer: Raman residual stress evaluation and AFM analyses. *Diamond and Related Materials*. 2012; 22: 105-12.
10. Mao WG, Chen Q, Dai CY, Yang L, Zhou YC and Lu C. Effects of piezo-spectroscopic coefficients of 8 wt.% Y2O3 stabilized ZrO2 on residual stress measurement of thermal barrier coatings by Raman spectroscopy. *Surface and Coatings Technology*. 2010; 204: 3573-7.
11. Liu D, Rinaldi C and Flewitt PEJ. Effect of substrate curvature on the evolution of microstructure and residual stresses in EBPVD-TBC. *J Eur Ceram Soc*. 2015; 35: 2563-75.
12. Wilkinson AJ and Britton TB. Strains, planes, and EBSD in materials science. *Materials Today*. 2012; 15: 366-76.
13. Kartal ME, Dunne FPE and Wilkinson AJ. Determination of the complete microscale residual stress tensor at a subsurface carbide particle in a single-crystal superalloy from free-surface EBSD. *Acta Mater*. 2012; 60: 5300-10.
14. Wilkinson A, Britton T, Jiang J and Karamched P. A review of advances and challenges in EBSD strain mapping. *IOP Conference Series: Materials Science and Engineering*. IOP Publishing, 2014, p. 012020.
15. Britton TB and Wilkinson AJ. Measurement of residual elastic strain and lattice rotations with high resolution electron backscatter diffraction. *Ultramicroscopy*. 2011; 111: 1395-404.
16. Khan MK, Fitzpatrick ME, Hainsworth SV, Evans AD and Edwards L. Application of synchrotron X-ray diffraction and nanoindentation for the determination of residual stress fields around scratches. *Acta Mater*. 2011; 59: 7508-20.
17. Suominen Fuller ML, Klassen RJ, McIntyre NS, et al. Texture, residual strain, and plastic deformation around scratches in alloy 600 using synchrotron X-ray Laue micro-diffraction. *J Nucl Mater*. 2008; 374: 482-7.

18. Meixner M, Klaus M and Genzel C. Sin2[psi]-based residual stress gradient analysis by energy-dispersive synchrotron diffraction constrained by small gauge volumes. I. Theoretical concept. *J Appl Crystallogr*. 2013; 46: 610-8.
19. Hofmann F, Abbey B, Song X, Dolbnya I and Korsunsky AM. Intragranular Lattice Misorientation Mapping by Synchrotron X-Ray Micro-Beams: Laue Vs Energy-Resolved Laue Vs Monochromatic Reciprocal Space Analysis. *Int J Mod Phys B*. 2010; 24: 279-87.
20. Hofmann F, Song X, Dolbnya I, Abbey B and Korsunsky AM. Probing intra-granular deformation by micro-beam Laue diffraction. *Procedia Engineer*. 2009; 1: 193-6.
21. Hofmann F, Song X, Jun TS, et al. High energy transmission micro-beam Laue synchrotron X-ray diffraction. *Mater Lett*. 2010; 64: 1302-5.
22. Cheng W and Finnie I. *Residual Stress Measurement and the Slitting Method*. New York, USA: Springer, 2007.
23. Liu C and Dong C-l. Internal residual stress measurement on linear friction welding of titanium alloy plates with contour method. *T Nonferr Metal Soc*. 2014; 24: 1387-92.
24. Kartal ME, Liljedahl CDM, Gungor S, Edwards L and Fitzpatrick ME. Determination of the profile of the complete residual stress tensor in a VPPA weld using the multi-axial contour method. *Acta Mater*. 2008; 56: 4417-28.
25. Schajer GS. Measurement of Non-Uniform Residual-Stresses Using the Hole-Drilling Method .1. Stress Calculation Procedures. *J Eng Mater Tech*. 1988; 110: 338-43.
26. Rendler NJ and Vigness I. Hole-drilling strain-gage method of measuring residual stresses. *Experimental Mechanics*. 1966; 6: 577-86.
27. Keil S. Experimental Determination of Residual Stresses with the Ring-Core Method and an On-line Measuring System. *Experimental Techniques*. 1992; 16: 17-24.
28. Park MJ, Yang HN, Jang DY, Kim JS and Jin TE. Residual stress measurement on welded specimen by neutron diffraction. *Journal of Materials Processing Technology*. 2004; 155–156: 1171-7.
29. Rogante M, Török G, Ceschini GF, Tognarelli L, Füzesy I and Rosta L. High-resolution diffraction for residual stress determination in the NiCrMoV wheel of an axial compressor for a heavy-duty gas turbine. *Physica B: Condensed Matter*. 2004; 350: E479-E81.
30. Wu H. 10 - Understanding residual stresses and fracture toughness in ceramic nanocomposites. In: Shokrieh MM, (ed.). *Residual Stresses in Composite Materials*. Woodhead Publishing, 2014, p. 256-92.
31. Snigireva I and Snigirev A. X-ray microanalytical techniques based on synchrotron radiation. *Journal of Environmental Monitoring*. 2006; 8: 33-42.
32. Vaughan GB, Wright JP, Bytchkov A, et al. X-ray transfocators: focusing devices based on compound refractive lenses. *Journal of synchrotron radiation*. 2011; 18: 125-33.
33. Malik A, Fox O, Alianelli L, et al. Deep reactive ion etching of silicon moulds for the fabrication of diamond x-ray focusing lenses. *Journal of Micromechanics and Microengineering*. 2013; 23: 125018.
34. Davies R. A new batch-processing data-reduction application for X-ray diffraction data. *J Appl Crystallogr*. 2006; 39: 267-72.
35. Roisnel T and Rodríquez-Carvajal J. WinPLOTR: a windows tool for powder diffraction pattern analysis. *Materials Science Forum*. Transtec Publications; 1999, 2001, p. 118-23.
36. Lutterotti L, Bortolotti M, Ischia G, Lonardelli I and Wenk H-R. Rietveld texture analysis from diffraction images. *Zeitschrift für Kristallographie Supplements*. 2007.

37. Toby BH. EXPGUI, a graphical user interface for GSAS. *J Appl Crystallogr*. 2001; 34: 210-3.
38. Song X, Xie M, Hofmann F, et al. Residual stresses in Linear Friction Welding of aluminium alloys. *Materials & Design*. 2013; 50: 360-9.
39. Xie M, Baimpas N, Reinhard C and Korsunsky A. Texture analysis in cubic phase polycrystals by single exposure synchrotron X-ray diffraction. *Journal of Applied Physics*. 2013; 114: 163502.
40. Sui T, Sandholzer MA, Lunt AJ, et al. In situ X-ray scattering evaluation of heat-induced ultrastructural changes in dental tissues and synthetic hydroxyapatite. *Journal of The Royal Society Interface*. 2014; 11: 20130928.
41. Al-Jawad M, Steuwer A, Kilcoyne SH, Shore RC, Cywinski R and Wood DJ. 2D mapping of texture and lattice parameters of dental enamel. *Biomaterials*. 2007; 28: 2908-14.
42. Low I, Duraman N and Mahmood U. Mapping the structure, composition and mechanical properties of human teeth. *Materials Science and Engineering: C*. 2008; 28: 243-7.
43. Tamura N, MacDowell A, Spolenak R, et al. Scanning X-ray microdiffraction with submicrometer white beam for strain/stress and orientation mapping in thin films. *Journal of synchrotron radiation*. 2003; 10: 137-43.
44. Kunz M, Tamura N, Chen K, et al. A dedicated superbend X-ray microdiffraction beamline for materials, geo-, and environmental sciences at the advanced light source. *Review of Scientific Instruments*. 2009; 80: 035108.
45. Leclere C, Cornelius TW, Ren Z, et al. In situ bending of an Au nanowire monitored by micro Laue diffraction. *J Appl Crystallogr*. 2015; 48: 291-6.
46. Robach O, Micha J-S, Ulrich O, et al. A tunable multicolourrainbow'filter for improved stress and dislocation density field mapping in polycrystals using X-ray Laue microdiffraction. *Acta Crystallographica Section A: Foundations of Crystallography*. 2013; 69: 164-70.
47. Hofmann F, Eve S, Belnoue J, Micha J-S and Korsunsky AM. Analysis of strain error sources in micro-beam Laue diffraction. *Nuclear Instruments and Methods in Physics Research Section A: Accelerators, Spectrometers, Detectors and Associated Equipment*. 2011; 660: 130-7.
48. Petit J, Bornert M, Hofmann F, et al. Combining Laue microdiffraction and digital image correlation for improved measurements of the elastic strain field with micrometer spatial resolution. *Procedia IUTAM*. 2012; 4: 133-43.
49. Sobiech M, Wohlschlögel M, Welzel U, et al. Local, submicron, strain gradients as the cause of Sn whisker growth. *Appl Phys Lett*. 2009; 94: 221901.
50. Abbey B, Hofmann F, Belnoue J, et al. Mapping the dislocation sub-structure of deformed polycrystalline Ni by scanning microbeam diffraction topography. *Scripta Mater*. 2011; 64: 884-7.
51. Poulsen HF, Wert JA, Neuefeind J, Honkimäki V and Daymond M. Measuring strain distributions in amorphous materials. *Nature Materials*. 2005; 4: 33-6.
52. Huang Y, Khong J, Connolley T and Mi J. In situ study of the evolution of atomic strain of bulk metallic glass and its effects on shear band formation. *Scripta Mater*. 2013; 69: 207-10.
53. Krieger Lassen NC, Juul Jensen D and Conradsen K. Image processing procedures for analysis of electron back scattering patterns. *Scanning Microscopy*. 1992; 6: 115-21.
54. Wilkinson AJ, Meaden G and Dingley DJ. High-resolution elastic strain measurement from electron backscatter diffraction patterns: new levels of sensitivity. *Ultramicroscopy*. 2006; 106: 307-13.

55. Keller R and Geiss R. Transmission EBSD from 10 nm domains in a scanning electron microscope. *Journal of Microscopy*. 2012; 245: 245-51.
56. Suzuki S. Features of transmission EBSD and its application. *Jom*. 2013; 65: 1254-63.
57. Vigouroux M, Delaye V, Bernier N, et al. Strain mapping at the nanoscale using precession electron diffraction in transmission electron microscope with off axis camera. *Appl Phys Lett*. 2014; 105: 191906.
58. Clément L, Pantel R, Kwakman LT and Rouvière J. Strain measurements by convergent-beam electron diffraction: The importance of stress relaxation in lamella preparations. *Appl Phys Lett*. 2004; 85: 651-3.
59. Roberts O, Lunt AJ, Ying S, et al. A Study of Phase Transformation at the Surface of a Zirconia Ceramic. *Proceedings of the World Congress on Engineering*. 2014.
60. Liu D, Kyaw S, Flewitt P, et al. Residual stresses in environmental and thermal barrier coatings on curved superalloy substrates: Experimental measurements and modelling. *Materials Science and Engineering: A*. 2014; 606: 117-26.
61. Kang Y, Qiu Y, Lei Z and Hu M. An application of Raman spectroscopy on the measurement of residual stress in porous silicon. *Optics and Lasers in Engineering*. 2005; 43: 847-55.
62. Correlative Raman-SEM Microscopy (RISE Microscopy) in Life Sciences. *Spectroscopy*. WITec GmbH, Feb 2015.
63. Korsunsky AM, Sebastiani M and Bemporad E. Focused ion beam ring drilling for residual stress evaluation. *Mater Lett*. 2009; 63: 1961-3.
64. Winiarski B, Gholinia A, Tian J, Yokoyama Y, Liaw PK and Withers PJ. Submicron-scale depth profiling of residual stress in amorphous materials by incremental focused ion beam slotting. *Acta Mater*. 2012; 60: 2337-49.
65. Wang Q, Ozaki K, Ishikawa H, Nakano S and Ogiso H. Indentation method to measure the residual stress induced by ion implantation. *Nucl Instr Meth Phys Res B*. 2006; 242: 88-92.
66. Oka Y, Kirinuki M, Nishimura Y, Azuma K, Fujiwara E and Yatsuzuka M. Measurement of residual stress in DLC films prepared by plasma-based ion implantation and deposition. *Surf Coat Tech*. 2004; 186: 141-5.
67. Prime MB. Residual stress measurement by successive extension of a slot: the crack compliance method. *Appl Mech Rev*. 1999; 52: 75-96.
68. Kang KJ, Yao N, He MY and Evans AG. A method for in situ measurement of the residual stress in thin films by using the focused ion beam. *Thin Solid Films*. 2003; 443: 71-7.
69. Sabate N, Vogel D, Gollhardt A, et al. Measurement of residual stress by slot milling with focused ion-beam equipment. *J Micromech Microeng*. 2006; 16: 254-9.
70. Sabaté N, Vogel D, Gollhardt A, et al. Measurement of residual stresses in micromachined structures in a microregion. *Appl Phys Lett*. 2006; 88: 071910.
71. Sabaté N, Vogel D, Keller J, et al. FIB-based technique for stress characterization on thin films for reliability purposes. *Microelectronic Engineering*. 2007; 84: 1783-7.
72. Mansilla C, Martínez-Martínez D, Ocelík V and De Hosson JTM. On the determination of local residual stress gradients by the slit milling method. *J Mater Sci*. 2015; 50: 3646-55.
73. Vogel D, Sabate N, Gollhardt A, Keller J, Auersperg J and Michel B. FIB-based measurement of local residual stresses on microsystems. 2006, p. 617505--8.
74. Winiarski B and Withers PJ. Mapping residual stress profiles at the micron scale using FIB micro-hole drilling. *Appl Mech Mater*. Trans Tech Publ, 2010, p. 267-72.

75. Winiarski B, Langford R, Tian J, Yokoyama Y, Liaw P and Withers P. Mapping Residual Stress Distributions at the Micron Scale in Amorphous Materials. *Metall Mater Trans A*. 2010; 41: 1743-51.
76. McCarthy J, Pei Z, Becker M and Atteridge D. FIB micromachined submicron thickness cantilevers for the study of thin film properties. *Thin Solid Films*. 2000; 358: 146-51.
77. Krottenthaler M, Schmid C, Schaufler J, Durst K and Göken M. A simple method for residual stress measurements in thin films by means of focused ion beam milling and digital image correlation. *Surf Coat Tech*. 2013; 215: 247-52.
78. Korsunsky AM, Sebastiani M and Bemporad E. Residual stress evaluation at the micrometer scale: Analysis of thin coatings by FIB milling and digital image correlation. *Surf Coat Tech*. 2010; 205: 2393-403.
79. Song X, Yeap KB, Zhu J, et al. Residual stress measurement in thin films at sub-micron scale using Focused Ion Beam milling and imaging. *Thin Solid Films*. 2012; 520: 2073-6.
80. Sebastiani M, Eberl C, Bemporad E and Pharr GM. Depth-resolved residual stress analysis of thin coatings by a new FIB–DIC method. *Materials Science and Engineering: A*. 2011; 528: 7901-8.
81. Song X, Yeap KB, Zhu J, et al. Residual stress measurement in thin films using the semi-destructive ring-core drilling method using Focused Ion Beam. *Procedia Engineering*. 2011; 10: 2190-5.
82. Lunt AJG and Korsunsky AM. Intragranular Residual Stress Evaluation Using the Semi-Destructive FIB-DIC Ring-Core Drilling Method. Advanced Materials Research2014, p. 8-13.
83. Korsunsky AM, Sebastiani M and Bemporad E. Residual stress evaluation at the micrometer scale: Analysis of thin coatings by FIB milling and digital image correlation. *Surface and Coatings Technology*. 2010; 205: 2393-403.
84. Gelfi M, Bemporad E, Mariangela B, et al. A critical comparison between XRD and FIB residual stress measurement techniques in thin films. *Surface and Coatings Technology or Thin Solid Films*. 2014.
85. Salvati E, Sui T, Ying S, Lunt AJ and Korsunsky AM. On the Accuracy of Residual Stress Evaluation from Focused Ion Beam DIC (FIB-DIC) Ring-core Milling Experiments. *Proceedings of ICNFA 2014*.
86. Martins RV, Ohms C and Decroos K. Full 3D spatially resolved mapping of residual strain in a 316L austenitic stainless steel weld specimen. *Materials Science and Engineering: A*. 2010; 527: 4779-87.
87. Zhu WL, Zhu JL, Nishino S and Pezzotti G. Spatially resolved Raman spectroscopy evaluation of residual stresses in 3C-SiC layer deposited on Si substrates with different crystallographic orientations. *Applied Surface Science*. 2006; 252: 2346-54.
88. Boyce BL, Chen X, Hutchinson JW and Ritchie RO. The residual stress state due to a spherical hard-body impact. *Mech Mater*. 2001; 33: 441-54.
89. Sebastiani M, Eberl C, Bemporad E, Korsunsky AM, Nix WD and Carassiti F. Focused ion beam four-slot milling for Poisson's ratio and residual stress evaluation at the micron scale. *Surf Coat Tech*. 2014; 251: 151-61.
90. Zhao W, Seshadri R and Dubey RN. On Thick-Walled Cylinder Under Internal Pressure. *Journal of Pressure Vessel Technology*. 2003; 125: 267-73.
91. Sahoo B, Satpathy RK, Prasad K, Ahmed S and Kumar V. Effect of Shot Peening on Low Cycle Fatigue Life of Compressor Disc of a Typical Fighter Class Aero-Engine. *Procedia Engineering*. 2013; 55: 144-8.

92. Sheng X-f, Xia Q-x, Cheng X-q and Lin L-s. Residual stress field induced by shot peening based on random-shots for 7075 aluminum alloy. *T Nonferr Metal Soc*. 2012; 22, Supplement 2: 261-7.
93. Song X, Liu W, Belnoue J, et al. An eigenstrain-based finite element model and the evolution of shot peening residual stresses during fatigue of GW103 magnesium alloy. *Int J Fatigue*. 2012; 42: 284-95.
94. Torres MAS and Voorwald HJC. An evaluation of shot peening, residual stress and stress relaxation on the fatigue life of AISI 4340 steel. *Int J Fatigue*. 2002; 24: 877-86.
95. Digital Image Correlation and Tracking, , http://www.mathworks.co.uk/matlabcentral/fileexchange/12413-digital-image-correlation-and-tracking. Accessed: : Dec 2012
96. Carpinteri A. *Structural Mechanics: A unified approach*. Abingdon, UK: Taylor & Francis, 2002.
97. Slama C and Abdellaoui M. Structural characterization of the aged Inconel 718. *J Alloy Compd*. 2000; 306: 277-84.
98. Mukherji D, Gilles R, Barbier B, et al. Lattice misfit measurement in Inconel 706 containing coherent γ′ and γ″ precipitates. *Scr Mater*. 2003; 48: 333-9.
99. Watanabe Y, Hasegawa N and Matsumura Y. Simulation of residual stress distribution on shot peening. *JSMS*. 1995; 44: 110-6.
100. King A, Johnson G, Engelberg D, Ludwig W and Marrow J. Observations of intergranular stress corrosion cracking in a grain-mapped polycrystal. *Science*. 2008; 321: 382-5.
101. Baimpas N, Lunt AJ, Dolbnya IP, Dluhos J and Korsunsky AM. Nano-scale mapping of lattice strain and orientation inside carbon core SiC fibres by synchrotron X-ray diffraction. *Carbon*. 2014; 79: 85-92.
102. Nelson DV. Residual Stress Determination by Hole Drilling Combined with Optical Methods. *Experimental Mechanics*. 2010; 50: 145-58.
103. Harris GL. *Properties of Silicon Carbide*. Stevenage, UK: INSPEC, IET, 1995.
104. Henson RW and Reynolds WN. Lattice parameter changes in irradiated graphite. *Carbon*. 1965; 3: 277-87.